Check for
updates

The improved photocatalytic capacity derived from AgI-modified mesoporous PANI spherical shell with open pores

Xueting Liu[1] · Hongcheng Zhu[1] · Jingjing Wu[1] · Fang Wang[1] · Fengyu Wei[1]

Abstract

Sulfonated polystyrene microspheres have been used as a template to produce a mesoporous polyaniline (M-PANI) spherical shell with open pores, based on which a novel visible-light-active AgI-modified M-PANI@AgI composite was prepared by a chemisorption method. The photocatalytic activity of M-PANI@AgI was significantly enhanced as compared to conventional PANI@AgI, and it increased with the increasing proportion of M-PANI. Superior stability was also observed in the cyclic runs, indicating that the as-prepared composite is highly desirable for the remediation of organic contaminated wastewaters. The improved photocatalytic performance is due to synergistic effects derived from the AgI-modified mesoporous PANI spherical shell with open pores, which can effectively accelerate the charge separation and reinforce the photostability of the composite. In addition, based on active species trapping experiments, a possible mechanism has been proposed.

✉ Fengyu Wei
  weifyliuj@163.com

1   School of Chemistry and Chemical Engineering, Anhui Key Laboratory of Controllable Chemical Reaction and Material Chemical Engineering, Hefei University of Technology, Hefei 230009, China

Graphical abstract
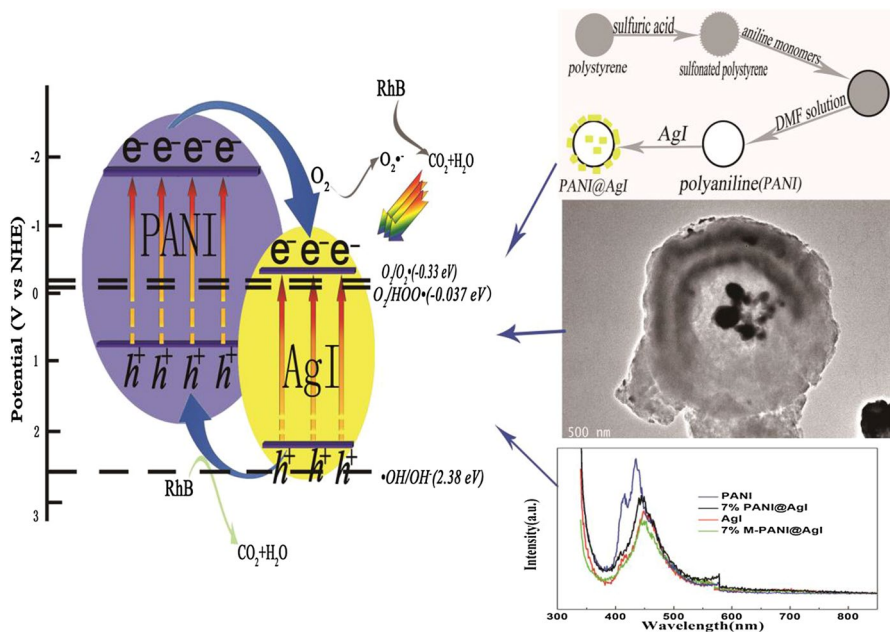
Keywords Microspheres · Polyaniline · AgI · Photocatalysis · Synergism

Introduction

Photocatalysis, as a promising green technology, has been extensively explored for potential applications in environmental remediation [1–5], CO_2 fixation [6, 7] and water splitting [8, 9]. TiO_2 is one of the most studied photocatalysts due to its multiple potential benefits of chemical stability, inexpensiveness, and non-toxic nature [10, 11]. However, TiO_2 can only be activated by ultraviolet light ($\lambda < 400$ nm), which makes up only about 4% of the solar spectrum. Therefore, it is crucial and a great challenge to explore efficient visible light-induced photocatalysts, an international hot topic in the field of photocatalysis.

Nowadays, delocalized π–π conjugated structures have been proven to induce a rapid photo-induced charge separation and to decrease the charge recombination rate in electron-transfer processes [12–15]. It is noteworthy that polyaniline (PANI) is one of the conductive polymers having the delocalized π–π conjugated structure, in which the benzenoid and quinonoid units have several redox states with many interesting properties [16]. PANI has displayed great potential in constructing various composite photocatalysts.

Silver halide (AgCl, AgBr and AgI)-based photocatalysts have been much explored in the photocatalysis field, due to their perfect activities in the photo-oxidation of organic pollutants [17, 18]; however, their stability is still low, and can be improved by combination with other materials. Here, we used monodispersed microsized sulfonated polystyrene (PS) spheres prepared by dispersion polymerization according to Paine et al. [19] as templates to prepare mesoporous polyaniline (M-PANI) spherical shells with open pores, and then AgI nanoparticles were adhered onto the surface and inner parts of M-PANI shells via a chemisorption method to yield a M-PANI@AgI composite photocatalyst [13]. M-PANI exhibited excellent absorption in the visible region. Moreover, the lowest unoccupied molecular orbital (LUMO) of PANI is -1.8 eV [20], which is more negative than the conduction band of AgI (-0.42 eV [21]). Since the reduction of RhB is through a successive one-electron process, it is thus thermodynamically feasible that the photogenerated electrons from M-PANI can be ultimately transferred to RhB through the conduction band of AgI. It is worth noting that the feature of AgI nanoparticles adhered on the surface and inner parts of M-PANI shells can increase the stability of AgI, and accelerate the charge separation via AgI-modified mesoporous PANI spherical shells by comparison with the conventional PANI@AgI. As a result, M-PANI spherical shells modified by AgI can exhibit improved photocatalytic capacity and good structural stability.

Experimental

Materials

Polyvinylpyrrolidone (PVP-K30) has a molecular mass of 44,000-54,000. Azoisobutyronitrile (AIBN; Aladdin Reagent) initiator was crystallized before being used. Styrene and aniline monomers were distilled under reduced pressure. N,N-dimethyl formamide (DMF), ferric chloride, silver nitrate, potassium iodide and concentrated sulfuric acid are of analytical grade without further purification. All reagents except AIBN used in this study were supplied by Sinopharm Chemical Reagent.

Synthesis of monodispersed polystyrene (PS) microspheres

A PS fine powder consisting of microspheres was prepared by dispersion polymerization according to Paine et al. [19]. The PVP stabilizer (1.0 g) was dissolved in ethanol (38.2 ml) in a three-necked round-bottom flask fitted with a condenser and a magnetic stirrer. The reaction vessel was then heated to 70 °C under a nitrogen blanket and purged with nitrogen for 12 h at 70 °C. A solution of AIBN (0.15 g) pre-dissolved in styrene monomer (15 g) was added to the reaction vessel with vigorous stirring. The styrene polymerization was allowed to proceed for 12 h before cooling to room temperature. The product was purified by repeated centrifugation and washed with ethanol. A fine white powder (PS) was finally obtained after being dried in a vacuum oven at 50 °C.

Preparation of sulfonated PS microspheres

After purification and drying, the PS fine powder (1.7 g) and concentrated sulfuric acid (98%, 60 ml) were introduced into a 100-ml conical flask. After ultrasonic dispersion, the sulfonation was allowed to take place at 40 °C under magnetic stirring for 5 h. When cooled to room temperature, the product was separated by repeated centrifugation (6000 rpm) and washed with a large excess of ethanol. Finally, a fine yellow powder (sulfonated PS) was obtained after being dried.

Preparation of hollow M-PANI microspheres

Sulfonated PS powder (0.1 g) was dispersed in water (10 mL) containing monomeric aniline (0.1 g) with stirring. After 2 h, aqueous ferric chloride (1 mol/l, 0.5 mL) was added to initiate oxidative polymerization at room temperature for 24 h. Mesoporous polyaniline spherical shells with open pores were obtained after centrifugation and treatment with DMF to dissolve the polystyrene.

Preparation of AgI

An amount of 20.0 mL aqueous solution of 0.34 g $AgNO_3$ was prepared. Then, 15.0 ml aqueous solution of 0.32 g KI was added into the above solution with stirring for 1 h at room temperature. After the reaction, the obtained precipitate was filtered, washed with deionized water and dried at 60 °C for 12 h. Finally, yellow AgI powder was obtained.

Preparation of M-PANI@AgI composite photocatalysts

The M-PANI@AgI composite photocatalysts was prepared as follows: M-PANI was dispersed in tetrahydrofuran to obtain a solution with a concentration of 0.45 g/L, then an amount of AgI powder was added to the above solution and then stirred for 24 h. The suspension was centrifuged and washed several times by distilled water and ethanol, and then transferred to oven to dry at 80 °C for 6 h. By this method, M-PANI@AgI photocatalysts with different PANI compouonds of 5, 7, 8 and 10 wt% were synthesized. The overall process for the fabrication of the AgI-modified mesoporous PANI spherical shell is shown in Scheme 1. For comparison, a 7% PANI@AgI composite photocatalyst using the same method but without using the PS template to construct a mesoporous structure was also prepared.

Photocatalytic experiments

The photocatalytic degradation of RhB was measured at ambient pressure and 298 K in a set of home-made photochemical reaction equipment. The light source was a PHILIPS 70-W metal halide lamp ($\lambda < 380$ nm was filtered out by a cut-off filter). Next, 20 mg of photocatalyst was added into 100 mL RhB (initial concentration, $C_0 = 10$ mg/L) aqueous solution. Before irradiation, the suspension was stirred continuously for 12 h in the
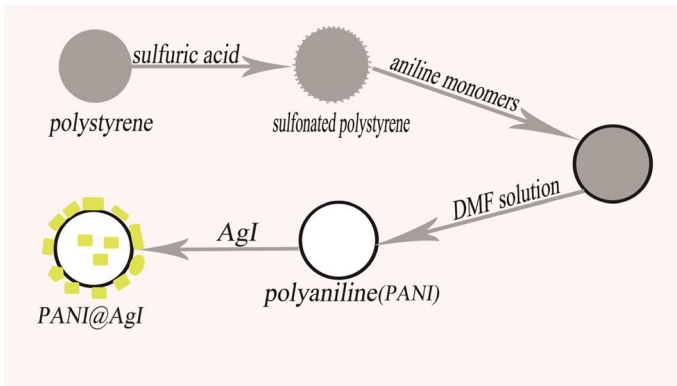
Scheme 1 Schematic illustration for the fabrication of M-PANI@AgI composites

dark in order to reach the adsorption–desorption equilibrium between the RhB and the photocatalyst. The supernatant liquid was obtained through filtration by 0.22-μm filter, and examined using a Shimadzu UV-240 spectrophotometer. For comparison, the photocatalytic activities of the as-prepared samples were also tested for the degradation of the colorless model pollutant phenol (10 mg/L) under the same conditions as with RhB.

Characterizations

A SU8020 field-emission scanning electron microscope (SEM) was used to characterize the surface morphologies of the PANI, the AgI and the PANI@AgI composite, while a transmission electron microscopy (TEM) image of M-PANI@AgI was obtained from a JEM-2100F (Japan). The crystal structures and phase states of the M-PANI@AgI composites were determined by X-ray diffractometry (XRD) using a Rigaku D/max-2500 V X-ray diffractometer with Cu-Ka ($\lambda = 0.154$ nm) radiation at an operating voltage of 40 kV and an operating current of 40 mA. N_2 adsorption–desorption (BET) was performed on a Tristar II3020 M surface area and porosity analyzer at 77 K. The infrared absorption spectra were investigated using a Fourier-transform infrared (FT-IR) spectrophotometer (Nicolet 67; USA) in the wave number range from 400 to 4000 cm^{-1}. X-ray photo-electron spectroscopy (XPS) measurements were performed on ESCALAB250 spectrometer to identify the elemental compositions and chemical states of M-PANI@AgI. UV–Vis spectra were recorded on a DUV-3700 spectrometer. Photoluminescence emission spectra (PL) were measured on a PL measurement system (Fluorolog Tau-3) with the excitation wavelength of 320 nm.

Results and discussion

The surface morphologies and average particle sizes of the PS template, the sulfonated PS template, M-PANI, AgI, PANI@AgI and M-PANI@AgI were examined by SEM and TEM measurements, and the results are shown in Fig. 1. Figure 1a

shows the unmodified PS microspheres, which have a smooth surface and uniform size with a diameter at about 1.3 μm. In addition, PVP-K30 was added before the start of the styrene polymerization reaction, and its main functions were dispersion stabilization, thickening, and particle size control. Figure 1b corresponds to a partially sulfonated sample having the functional groups (–SO$_3$H), and the size of spheres is not changed too much because the sulfonation reaction occurs inwardly from the PS particles' surface [22]. Nevertheless, its surface characteristic is different from that of the unsulfonated sample. Figure 1c is the SEM image of the M-PANI that have open pores on their spherical shells. AgI samples (Fig. 1d) are mainly composed of irregular particles with diameters between 0.4 and 1.5 μm. Figure 1e reveals that, after coupling AgI with PANI, the morphology and size of the
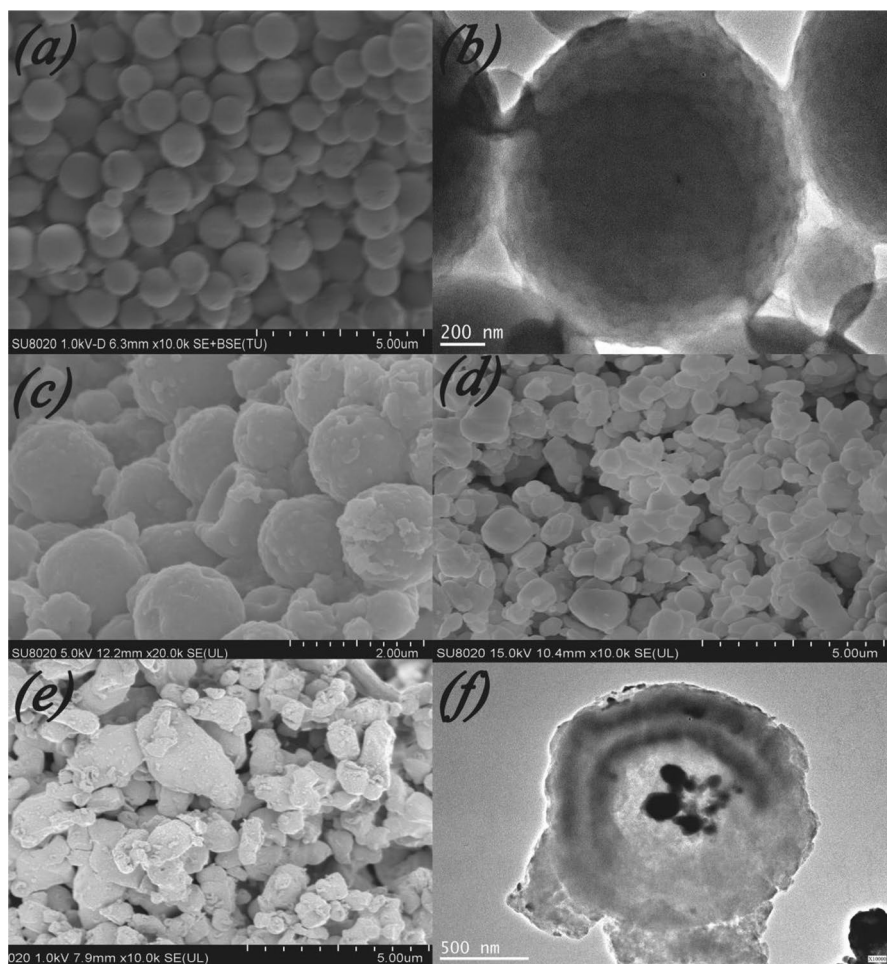

Fig. 1 SEM image of PS template (**a**) and TEM image of sulfonated PS template (**b**); SEM images of M-PANI (**c**), AgI particles (**d**) and PANI@AgI (**e**); TEM image of M-PANI@AgI (**f**)

resulting PANI@AgI composite is still similar to AgI. Figure 1f is the SEM image of the M-PANI@AgI composite, from which it can be clearly seen that the AgI nanoparticles are adhered on the surface and inner parts of the M-PANI spherical shells with open pore. It can be suggested that, during the preparation of M-PANI@AgI composite, a portion of AgI particles entered into PANI spherical shells via open pore. The rough and mesoporous surface of M-PANI@AgI is very beneficial to the propagation of visible light in the photocatalyst [23]. Moreover, this unique structure of M-PANI@AgI allows multiple reflections or scattering of light within the interior void, which could lead to a more efficient use of the visible light. Meanwhile, these characteristics are especially beneficial to the intimate contact between M-PANI and AgI, and can enhance the stability of the resulting composite. As a result, the efficient separation of photogenerated charge-carriers and the corresponding high photocatalytic capacity can be obtained.

Figure 2 shows the XRD patterns of AgI and 7% M-PANI@AgI. For AgI, the diffraction peaks at approximately 22°, 23°, 25°, 39°, 42°and 46° are indexed to (100), (002), (101), (110), (200) and (112) crystal planes of the hexagonal β-AgI crystal phase (JCPDS card no.09-0374), respectively [24]. The XRD patterns of 7% M-PANI@AgI hardly changed in the peak positions and shapes compared with those of AgI, indicating that, after adhering on M-PANI, the lattice structure of AgI is stable, which will be beneficial for the photocatalysis of the as-prepared composite photocatalyst.

The liquid N_2 adsorption–desorption isotherms and corresponding pore size distribution curves of 7% PANI@AgI and 7% M-PANI@AgI composites are depicted in Fig. 3a and b. The isotherm of 7% M-PANI@AgI composite is type IV according to IUPAC [25], and this finding demonstrates the existence of mesopores in 7% M-PANI@AgI, and its pore diameter ranges from 2 nm to 20 nm (Fig. 3b); however, by comparison, there are no mesopores for 7% PANI@AgI. The mesopores in 7% M-PANI@AgI can be derived from the use of the template of mesoporous PS to prepare mesoporous polyaniline. The large pore size in 7% M-PANI@AgI can enhance the adsorption and reaction for pollutants on surface active sites, and this phenomenon favors the enhancement in photocatalytic activity.

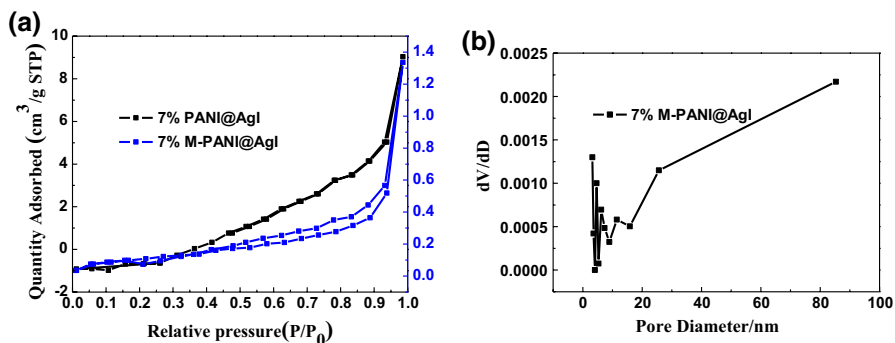**Fig. 2** X-ray diffraction patterns of AgI and 7% M-PANI@AgI
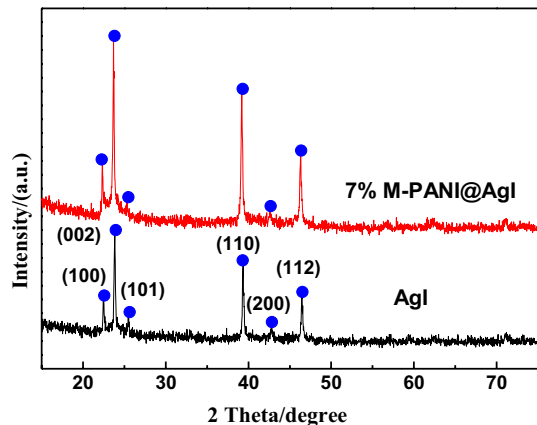
Fig. 3 **a** The N_2 adsorption–desorption isotherms of 7% PANI@AgI and 7% M-PANI@AgI; **b** the BJH pore diameter distribution curve of 7% M-PANI@AgI

FT-IR has been used to verify the interaction between AgI and M-PANI (Fig. 4). The peaks at 1570 cm^{-1} and 1487 cm^{-1} are identified as C=N and C=C stretching deformations of quinoid and benzenoid rings, respectively. The peak at 1138 cm^{-1} is the C–H in-plane bending vibration, and the bands at 2919 and 3047 cm^{-1} are assigned to the C–H stretching mode in the benzene rings [26, 27]. The peaks at 1296 cm^{-1} and 796 cm^{-1} correspond to the C–N stretching vibration mode and the N–H out-of-plane deformation vibration mode, respectively [28], while the typical peaks of 7% M-PANI@AgI are similar to those of PANI, except for the decrease in intensity. Indeed, the chemical bonds are influenced due to the interaction between AgI and the surface dangling bonds of M-PANI. C=N, C–N and C–H become weaker, and provide the evidence that the M-PANI conjugated bond was stretched and a more conjugated structure containing PANI and AgI was formed. A similar chemical bonding was also observed in the case of the ZnO [29] and TiO$_2$ [13]
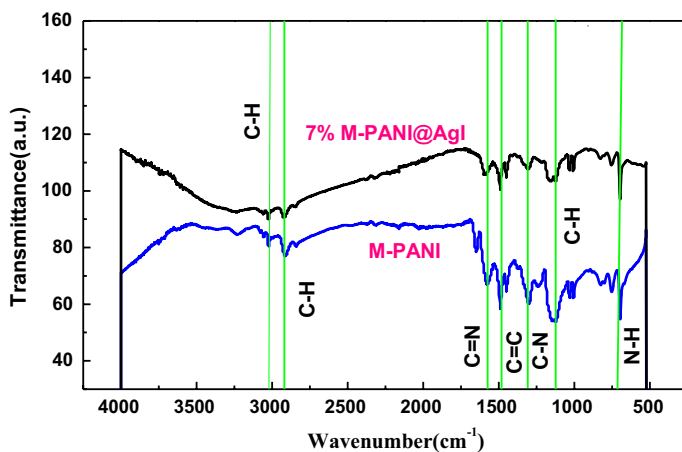

Fig. 4 FT-IR spectra of M-PANI and 7% M-PANI@AgI

hybrid monolayer polyaniline composites, as reported by Zhu et al. The AgI-modified M-PANI conjugated shell structure is essential to promote the separation efficiency of photo-generated carriers and to enhance the photocatalytic activity and anti-photocorrosion performance of M-PANI@AgI photocatalyst.

The chemical composition and surface chemical states of AgI and the 7% M-PANI@AgI composite were analyzed by XPS. As shown in Fig. 5, the XPS spectra of Ag species in the composite display two peaks at approximately 368.4 and 374.4 eV, which correspond to the binding energies of Ag $3d_{5/2}$ and Ag $3d_{3/2}$ of Ag, respectively. (Fig. 5a) [30, 31]. The I3d$_{5/2}$ and I3d$_{3/2}$ peaks of AgI are located at 619.8 and 631.3 eV (Fig. 5b), respectively, indicating the monovalent oxidation state of iodine [32, 33], and the peaks of I for the 7% M-PANI@AgI composite shift to 619.6 eV and 631.1 eV. It may be concluded that there was an intense interfacial interaction between M-PANI and AgI [34]. The binding energies of the three typical peaks of C 1 s of 7% M-PANI@AgI are at 284.7, 285.3 and 286.8 eV (Fig. 5c), corresponding to C–H or C=C, C–N and C=N, respectively [35]. The N 1 s spectrum of 7% M-PANI@AgI represents quinonoid diimine at 398.9 eV, benzenoid imine at 399.7 eV, and protonation imine at 400.8 eV (Fig. 5d) [36]. These observations further confirm that the incorporation of AgI into the M-PANI photocatalyst could substantially enhance the stability of AgI.

Considering that the visible-light absorption property plays an essential role in determining the visible photocatalytic performance of photocatalysts, the UV–Vis diffuse reflectance spectra were determined. Figure 6a shows the UV–Vis spectra of
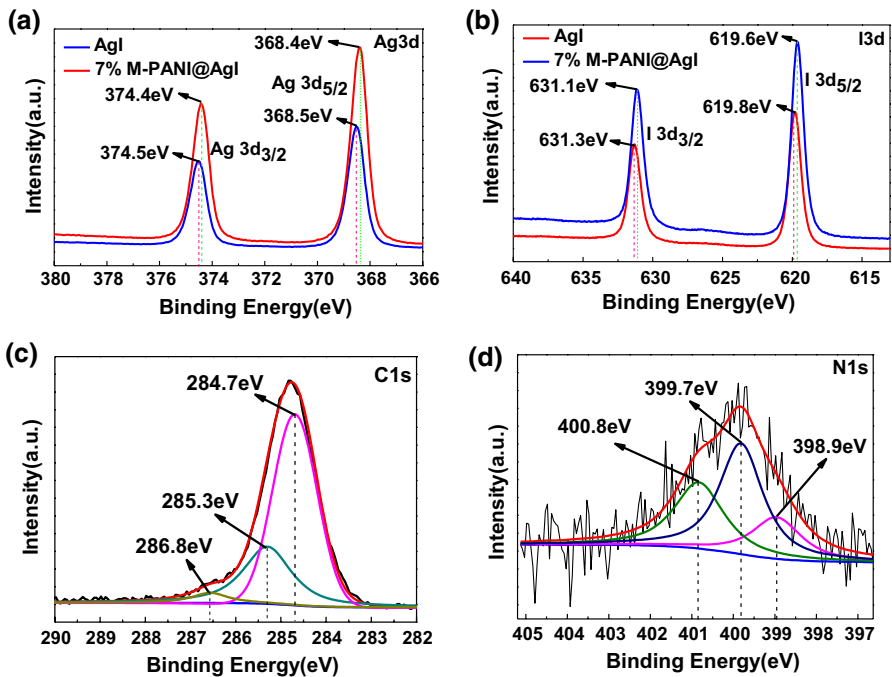

Fig. 5 XPS spectra of AgI and 7% M-PANI@AgI composite: **a** Ag3d, **b** I3d, **c** C1 s, **d** N 1 s

the as-prepared pure AgI, M-PANI and 7% M-PANI@AgI composite. Pure AgI has an absorption onset at 445 nm, which corresponds to a band gap of 2.79 eV as determined by the Kubelka–Munk theory (Inset of Fig. 6b) [36]. The 7% M-PANI@AgI composite shows significantly stronger light absorption than AgI. The transition band gap estimated from the onset of the curve edge is about 2.78 eV. The relatively narrow band-gap energy observed for 7% M-PANI@AgI is likely attributed to the strong interaction of the hybrid structure, which enables more efficient utilization of the solar spectrum. Furthermore, the formation of a conjugated structure between M-PANI and AgI over a wide range facilitates the migration efficiency of photo-induced charges and suppresses the charge recombination, thus enhancing the photocatalytic performance of M-PANI@AgI.

The photoluminescence (PL) spectrum is often used to study the separation efficiency of the photogenerated electron–hole pairs in semiconductor particles [37, 38]. Figure 7 shows the PL spectra of PANI, 7% PANI@AgI, AgI and 7% M-PANI@AgI, and all the samples show similar PL emissions in the range of 400–550 nm, while the order of the PL spectra intensities is as follows: PANI > 7% PANI@AgI > AgI > 7% M-PANI@AgI. The peak intensity of 7% M-PANI@AgI is much lower than those of pure AgI and 7% PANI@AgI, and displays the weakest PL emission. In general, the 7% M-PANI@AgI sample holds the best capability in charge separation. The remarkable reduction of PL intensity implies a high charge separation rate. This shows that mesoporous PANI can certainly suppress the recombination process of the photogenerated electron–hole pairs. As displayed in Fig. 1f, the mesoporous spherical shell having open pores with AgI particles adhered on the surface or innew part of the 7% M-PANI@AgI composite may be responsible for this low PL emission, because more contact interfaces exist between M-PANI and AgI as compared with those in 7% PANI@AgI without a mesoporous spherical shell.

The adsorption performance of pure materials and composites was studied (Fig. 8). The adsorbed quantity, q_e, can be calculated using the following relationship:
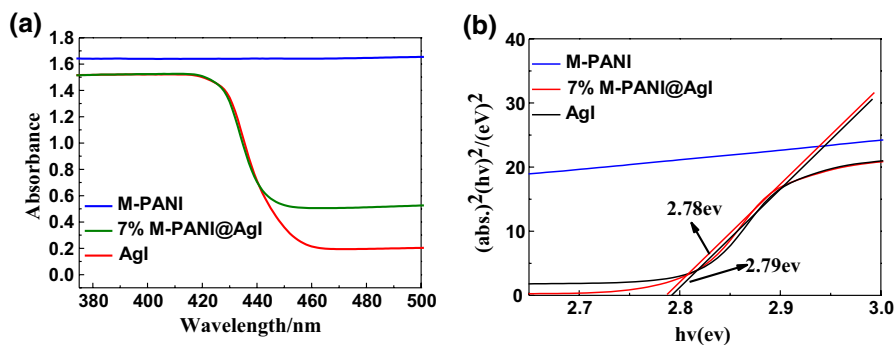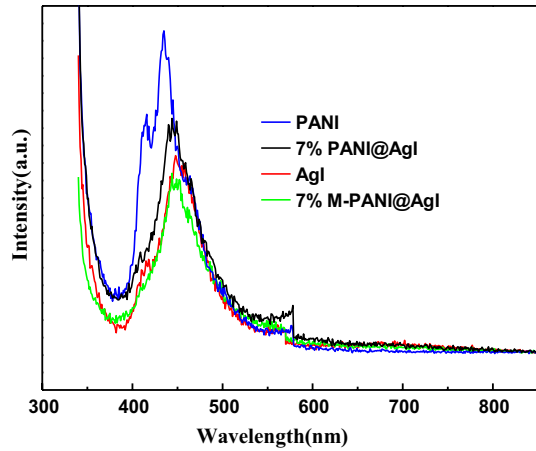
$$q_e = \frac{V(C_0 - C_e)}{m} \tag{1}$$

Fig. 6 UV–Vis spectra of **a** AgI, M-PANI and 7% M-PANI@AgI composite, and **b** the estimated band gap of AgI and 7% M-PANI@AgI

Fig. 7 PL emission spectra for PANI, 7% PANI@AgI, AgI and 7% M-PANI@AgI

where q_e (mg/g) is the amount of dye adsorbed onto the adsorbent at equilibrium, with C_0 and C_e (mg/L) denoting the liquid-phase concentrations of dye at initial and equilibrium, and V (L) and m (g) as the volume of dye solution and the mass of adsorbent, respectively. M-PANI displays a higher adsorption capacity of RhB in contrast with AgI (Fig. 8). This is due to the large BET surface area and the mesoporous structure of M-PANI and the electrostatic attraction interaction between RhB and M-PANI [39]. Meanwhile, the adsorption of RhB onto the M-PANI@
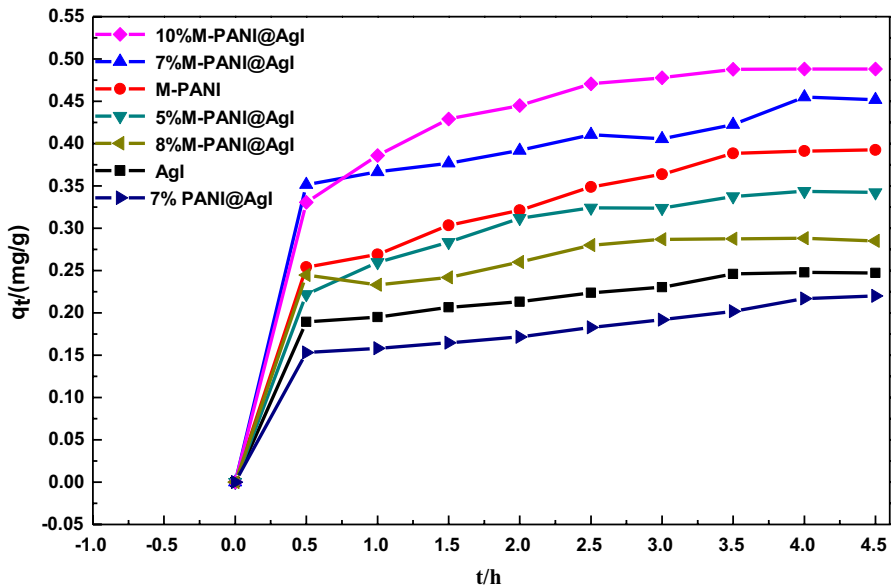

Fig. 8 Adsorption capacity of RhB onto 10% M-PANI@AgI, 7% M-PANI@AgI, M-PANI, 8% M-PANI@AgI, 5% M-PANI@AgI, AgI and 7% PANI@AgI

AgI composite has a great advantage as compared with that onto AgI, because M-PANI@AgI has a much larger specific surface area than conventional PANI and AgI nanoparticles. Thus, the M-PANI@AgI composite can offer more active adsorption sites, and display enhanced adsorption capacity for RhB.

The photocatalytic capability of AgI, M-PANI, and M-PANI@AgI with different mass ratios under visible light illumination ($\lambda > 400$ nm) was evaluated by comparing the photodegradation efficiency of RhB as presented in Fig. 9a. During 3.0 h of illumination, the optimal photocatalytic capability was achieved when the proportion of M-PANI reached 7% with the photodegradation efficiency being 99.64%. However, when the proportion of M-PANI exceeded 7%, the photocatalytic capability of M-PANI@AgI samples decreased and 93.28% of RhB was photodegraded for 8% M-PANI@AgI. This is because, when the ratio of M-PANI surpassed 7%, the superfluous mesoporous PANI molecules may impede the transfer of the photo-induced carriers and separation of electron–hole pairs [13]. The mesoporous structure in M-PANI@AgI composite photocatalyst is vital for the improved photocatalytic capacity. To confirm this assumption, the photocatalytic capability of 7% PANI@AgI was investigated and 53.98% of RhB was photodegraded by 7% PANI@AgI in 3.0 h, which was only 0.54 times that with 7% M-PANI@AgI. The kinetic behaviors of the as-prepared samples for photodegradation of RhB were investigated further, and all of them fit well with the pseudo-first-order correlation: $\ln(c_0/c) = kt$, where C is the concentration of RhB remaining in the solution at an irradiation time of t, C_0 is the initial concentration at $t = 0$, and k is the degradation apparent rate constant. The k values of different samples are shown in Fig. 9b, and, under the same experimental condition, the k values decrease as follows: 7% M-PANI@AgI > 5% M-PANI@AgI > 10% M-PANI@AgI > 8% M-PANI@AgI > 7% PANI@AgI > AgI > M-PANI. Obviously, the kinetic constant shows that 7% M-PANI@AgI has the best photocatalytic activity.

In addition, phenol, as a colorless substance without absorbtion of visible light, was used as the second model pollutant to further evaluate the photocatalytic performance of the as-prepared samples under visible light, and the obtained results are illustrated in Fig. 9c. It is clear that the photodegradation efficiency follows the same order: 7% M-PANI@AgI > 7% PANI@AgI > AgI > M-PANI, as compared to the photodegradation of RhB. After 6.0 h of irradiation, about 45% percent of the phenol was removed over the 7% M-PANI@AgI composite. By comparing Fig. 9a with Fig. 9c, one can see that the photocatalytic activity for phenol is lower than that for RhB. This phenomenon is often observed in photocatalytic studies.

The regeneration of the photocatalyst is one of the important steps for practical applications. To evaluate the photocatalytic stability, 7% M-PANI@AgI sample was reused in five successive degradation experiments. As shown in Fig. 10a, the photocatalytic activity of 7% M-PANI@AgI remains almost the same in the first two experimental runs but decreases in the third run, and, after the five rounds of circulation, the k value stabilizes at about 1.63 h^{-1}, which is 90.5% of the first cycle. Besides the cycle experiment, the good structural stability of PANI@AgI can also be confirmed by the XRD patterns (Fig. 10b) which indicate that the structure or integrity of the photocatalyst changes little after the photocatalytic process.

Fig. 9 Process of photocatalytic degradation of RhB under visible light irradiation: **a** 7% M-PANI@AgI, 5% M-PANI@AgI, 10% M-PANI@AgI, 8% M-PANI@AgI, 7% PANI@AgI, AgI, M-PANI; **b** the apparent rate constants for RhB degradation. Process of photocatalytic degradation of phenol (10 mg/L) under visible light irradiation **c** 7% M-PANI@AgI, 7% PANI@AgI, AgI, M-PANI
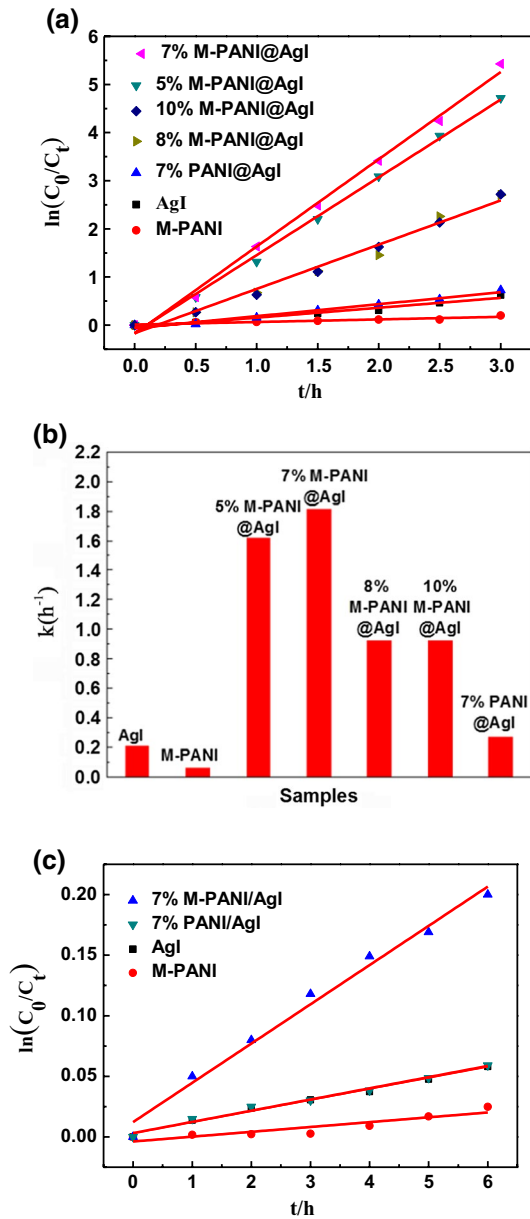
Photocatalytic mechanism of M-PANI@AgI

The different active species trapping experiments for the degradation of RhB over the 7% M-PANI@AgI composite were carried out to explore the enhanced photocatalytic mechanism, in which tertiary butyl alcohol (t-BuOH), ammonium oxalate (AO), and benzoquinone (BQ) acting as the scavengers for ·OH [40], h+ [41–43],
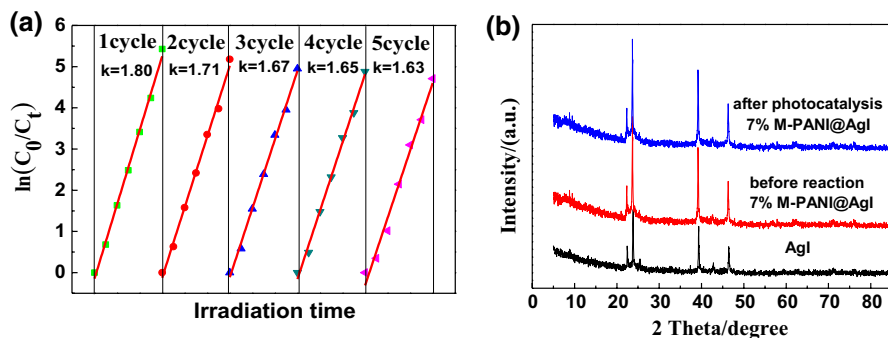
Fig. 10 **a** Repeated adsorption and photocatalytic degradation of RhB by 7% M-PANI@AgI under visible light; **b** XRD patterns of 7% M-PANI@AgI before and after photocatalysis

and O_2^- [44], respectively, were introduced into the photocatalytic oxidation process. As shown in Fig. 11, the addition of t-BuOH in the RhB solution has little effect on the photocatalytic activity of 7% M-PANI@AgI, suggesting that ·OH does not play a key role for the degradation of RhB. On the contrary, the RhB decomposition process was significantly inhibited by BQ and AO. On the basis of these results, it can be concluded that O_2^- and h^+ are the main active oxidation species for 7% M-PANI@AgI in the RhB solution under visible light irradiation.

Through SEM, TEM, the N_2 adsorption–desorption isotherms and the BJH pore diameter distribution curves test, it can be suggested that, when the AgI nanoparticles were adhered on the surface and innew part of M-PANI spherical shells, more active adsorption sites were offered for M-PANI@AgI than for PANI@AgI, and the interfacial photoreaction was enhanced. On the other hand, the mesoporous spherical shell structure of PANI facilitated the propagation of light waves in the photocatalyst and increased the optical path length in the photocatalyst by multiple reflections and scattering of visible light within the interior cavity. Third, the unique structure of M-PANI@AgI especially with AgI adhered in the inner part

Fig. 11 Photocatalytic activities of 7% M-PANI@AgI on the degradation of RhB in the presence of different scavengers under visible light irradiation (> 420 nm)
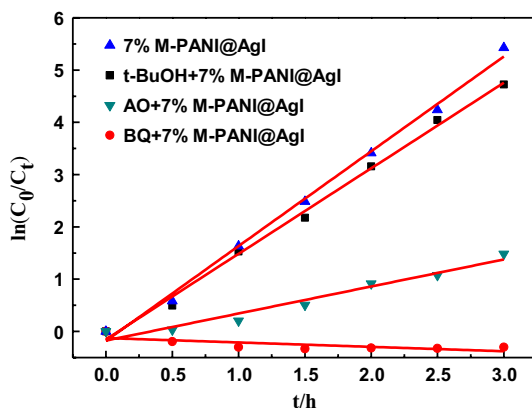
of the M-PANI spherical shells may protect AgI and contribute to its high stability in the composite. On the basis of the above analysis, a possible mechanism for the degradation of RhB by the M-PANI@AgI composite under visible irradiation is proposed in Scheme 2. When irradiated under visible light, M-PANI@AgI can induce the π–π* transition, delivering the excited-state electrons of the highest occupied molecular orbital (HOMO) orbital to the LUMO orbital [45]. The LUMO and HOMO potentials of PANI are -1.9 and 0.8 eV, respectively, and the conduction band (CB) and the valence band (VB) of AgI are -0.42 eV and 2.35 eV, respectively [20, 22]. Since the LUMO potential of PANI is more negative than the CB of AgI, and on the basis of the synergistic effect, the photogenerated electrons of PANI can be directly injected into the CB of AgI through the well-defined interface, and the conduction band of AgI is more negative than the standard redox potential of $O_2/O_2^-(-0.33$ eV$)$ [46]; then, the electrons on the CB of AgI can react with oxygen molecules to generate O_2^- radicals [47]. At the same time, holes in the VB of AgI migrate to the HOMO of PANI, and are involved in the direct oxidation of RhB to CO_2 and H_2O. In this situation, PANI itself is not only an electron donor but also the hole acceptor, and then a circulatory system between M-PANI and AgI will form when M-PANI@AgI is exposed to light. Therefore, a series of active species such as O_2^- and h^+ were successively generated in the photocatalytic process, thereby enhancing the photocatalytic activity of the M-PANI@AgI photocatalyst. Compared with PANI@AgI, the higher photocatalytic capacity of M-PANI@AgI should be the result of synergism including large adsorption capacity, efficient utilization of visible light and high charge separation rate, all of which are derived from the unique structure of AgI-modified mesoporous PANI spherical shells with open pores.
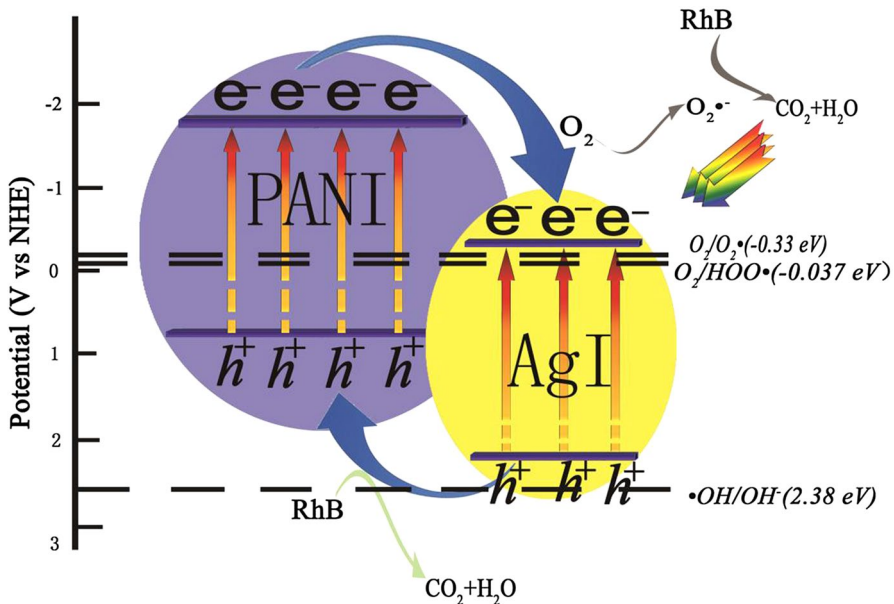
Scheme 2 Mechanism diagram of the RhB photodegradation on M-PANI@AgI

Conclusions

In this study, a novel visible-light-driven M-PANI@AgI photocatalyst was successfully prepared by a chemisorption method. SEM, TEM, XRD, the N_2 adsorption–desorption isotherms, FT-IR, XPS, UV–Vis and PL characterizations have been conducted on the M-PANI@AgI. AgI-modified mesoporous PANI spherical shell with open pores in M-PANI@AgI showing multiple advantages over PANI@AgI on the photocatalytic degradation of RhB and phenol under visible-light irradiation. The mesoporous PANI spherical shell with open pored can act as a platform to construct other high-efficiency composite photocatalysts in future research.

References

1. C. Chen, W. Ma, J. Zhao, Chem. Soc. Rev. **39**, 4206 (2010)
2. Z. Guan, G. Kim, W. Choi, Energ. Environ. Sci. **7**, 954 (2014)
3. S. Kim, J. Yeo, W. Choi, Appl. Catal. B Environ. **84**, 148 (2008)
4. X. Li, Y. Huang, J.F. Chen, X. Tao, Catal. Commun. **20**, 94 (2012)
5. L. Zhang, D. Jing, X. She, H. Liu, D. Yang, Y. Lu, J. Li, Z. Zheng, L. Guo, J. Mater. Chem. **2**, 2071 (2013)
6. M. Mikkelsen, Energ. Environ. Sci. **3**, 43 (2010)
7. F. Sastre, A.V. Puga, L. Liu, A. Corma, H. García, J. Am. Chem. Soc. **136**, 6798 (2014)
8. Y. Cong, M. Chen, T. Xu, Y. Zhang, Q. Wang, Appl. Catal. B Environ. **147**, 733 (2014)
9. Y. Zhang, S. Jiang, S. Song, P. Zhou, H. Ji, W. Ma, W. Hao, C. Chen, J. Zhao, Energ. Environ. Sci. **8**, 1231 (2015)
10. Y.P. Yuan, S.W. Cao, Y.S. Liao, L.S. Yin, C. Xue, Appl. Catal. B Environ. **140–141**, 164 (2013)
11. M. Pelaez, N.T. Nolan, S.C. Pillai, M.K. Seery, P. Falaras, A.G. Kontos, P.S.M. Dunlop, Appl. Catal. B Environ. **125**, 331 (2012)
12. G. Yu, J. Gao, J.C. Hummelen, F. Wudl, A.J. Heeger, Science **270**, 1789 (1995)
13. Z. Zhang, R. Zong, J. Zhao, Y. Zhu, Environ. Sci. Technol. **42**, 3803 (2008)
14. J. Wang, W. Jiang, L. Di, W. Zhen, Y. Zhu, Appl. Catal. B Environ. **176–177**, 306 (2015)
15. B.Y. Xia, H.B. Wu, J.S. Chen, Z. Wang, X. Wang, X.W. Lou, Phys. Chem. Chem. Phys. **14**, 473 (2011)
16. M. Nandi, R. Gangopadhyay, A. Bhaumik, Microporous Mesoporous Mater. **109**, 239 (2008)
17. H. Yu, L. Xu, P. Wang, X. Wang, J. Yu, Appl. Catal. B Environ. **144**, 75 (2014)
18. W. Zhao, G. Yang, S. Wang, H. He, C. Sun, S. Yang, Appl. Catal. B Environ. **165**, 335 (2015)
19. A.J. Paine, Macromolecules **23**, 157 (2002)
20. W. Wu, S. Liang, L. Shen, Z. Ding, H. Zheng, W. Su, J. Alloy. Compd. **520**, 213 (2012)
21. H. Cheng, W. Wang, B. Huang, Z. Wang, J. Zhan, X. Qin, X. Zhang, Y. Dai, J. Mater. Chem. A **1**, 7131 (2013)
22. Z. Yang, D. Li, J. Rong, W. Yan, Z. Niu, Macromol. Mater. Eng. **287**, 627 (2002)
23. X. Wang, J.C. Yu, C. Ho, Y. Hou, X. Fu, Langmuir **21**, 2552 (2005)
24. Y. Xu, H. Xu, J. Yan, H. Li, L. Huang, J. Xia, S. Yin, H. Shu, Colloid. Surf. A **436**, 474 (2013)
25. G. Liao, S. Chen, X. Quan, Y. Zhang, H. Zhao, Appl. Catal. B Environ. **102**, 126 (2011)
26. S.V. Awate, R.K. Sahu, M.D. Kadgaonkar, R. Kumar, N.M. Gupta, Catal. Today **141**, 144 (2009)
27. N.S. And, S. Vasudevan, J. Phys. Chem. B **108**, 11585 (2004)
28. K. He, M. Li, L. Guo, Int. J. Hydrogen Energ. **37**, 755 (2012)
29. H. Zhang, R. Zong, Y. Zhu, J. Phys. Chem. C **113**, 4605 (2014)
30. C. Hu, X. Hu, L. Wang, J. Qu, A. Wang, Environ. Sci. Technol. **40**, 7903 (2006)

31. Y. Zhang, Z.R. Tang, X. Fu, Y.J. Xu, Appl. Catal.B Environ. **106**, 445 (2011)
32. C. Liang, K. Terabe, T. Tsuruoka, M. Osada, T. Hasegawa, M. Aono, Adv. Funct. Mater. **17**, 1466 (2007)
33. Y. Xu, S. Huang, H. Ji, L. Jing, M. He, H. Xu, Q. Zhang, H. Li, RSC Adv. **6**, 6905 (2016)
34. M.T. Greiner, M.G. Helander, W.M. Tang, Z.B. Wang, J. Qiu, Nat. Mater. **11**, 76 (2012)
35. N. Wang, J. Li, W. Lv, J. Feng, W. Yan, RSC Adv. **5**, 21132 (2015)
36. R. Mohini, N. Lakshminarasimhan, Mater. Res. Bull. **76**, 370 (2016)
37. P. Zhao, D.S. Liu, Y. Zhang, Y. Su, H.Y. Liu, S.J. Li, G. Chen, J. Phys. Chem. C **116**, 7968 (2012)
38. G.K.R. Senadeera, T. Kitamura, Y. Wada, S. Yanagida, J. Photoch. Photobio. A **164**, 61 (2004)
39. Q. Chen, Q. He, M. Lv, Y. Xu, H. Yang, X. Liu, F. Wei, Appl. Surf. Sci. **327**, 77 (2015)
40. D. Chen, Z. Jiang, J. Geng, A. Qun Wang, D. Yang, Ind. Eng. Chem. Res. **46**, 2741 (2007)
41. P. Xiong, Q. Chen, M. He, X. Sun, X. Wang, J. Mater. Chem. **22**, 17485 (2012)
42. X. Pan, L. Wang, X. Sun, X. Binhai, W. Xin, Ind. Eng. Chem. Res. **52**, 10105 (2013)
43. Q. Chen, Q. He, M. Lv, X. Liu, J. Wang, J. Lv, Appl. Surf. Sci. **311**, 230 (2014)
44. L. Mohapatra, K. Parida, M. Satpathy, J. Phys. Chem. C **116**, 13063 (2012)
45. L. Zhang, M. Wan, J. Phys. Chem. B **107**, 6748 (2003)
46. J.O.M. Bockris, J. Bard, R. Faulkner, J. Electroanal. Chem. **125**, 255 (1981)
47. J. Ma, Q. Liu, L. Zhu, Z. Jing, W. Kai, M. Yang, Appl. Catal. B Environ. **182**, 26 (2016)